JACS
JOURNAL OF THE AMERICAN CHEMICAL SOCIETY
pubs.acs.org/JACS
Article

Transformation of $K_2Sb_8Q_{13}$ and KSb_5Q_8 Bulk Crystals to Sb_2Q_3 (Q = S, Se) Nanofibers by Acid−Base Solution Chemistry

Hyungseok Lee, Byeongjun Yoo, Dawoon Kim, Joonil Cha, Yeo Kyung Kang, Sung-Pyo Cho, Taeghwan Hyeon, Myung-Gil Kim,* Mercouri G. Kanatzidis,* and In Chung*

Cite This: J. Am. Chem. Soc. 2023, 145, 15951−15962
Read Online

ABSTRACT: The ability to manipulate crystal structures using kinetic control is of broad interest because it enables the design of materials with structures, compositions, and morphologies that may otherwise be unattainable. Herein, we report the low-temperature structural transformation of bulk inorganic crystals driven by hard−soft acid−base (HSAB) chemistry. We show that the three-dimensional framework $K_2Sb_8Q_{13}$ and layered KSb_5Q_8 (Q = S, Se, and Se/S solid solutions) compounds transform to one-dimensional Sb_2Q_3 nano/microfibers in $N_2H_4{\cdot}H_2O$ solution by releasing Q^{2-} and K^+ ions. At 100 °C and ambient pressure, a transformation process takes place that leads to significant structural changes in the materials, including the formation and breakage of covalent bonds between Sb and Q. Despite the insolubility of the starting crystals in $N_2H_4{\cdot}H_2O$ under the given conditions, the mechanism of this transformation can be rationalized by applying the HSAB principle. By adjusting factors such as the reactants' acid/base properties, temperature, and pressure, the process can be controlled, allowing for the achievement of a wide range of optical band gaps (ranging from 1.14 to 1.59 eV) while maintaining the solid solution nature of the anion sublattice in the Sb_2Q_3 nanofibers.

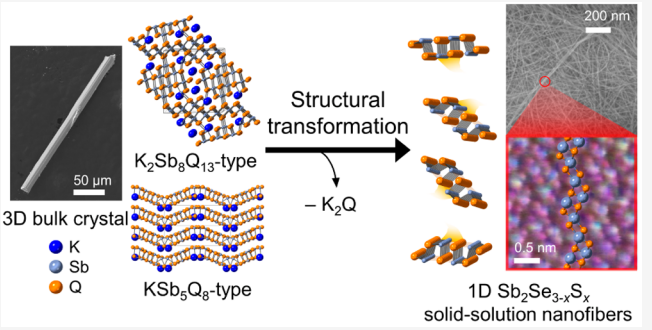

INTRODUCTION

Solid-state synthesis involves high temperatures to form new chemical bonds and create stable product phases, but controlling the reaction process to achieve desired structures is challenging due to the complex nature of solid-state materials.[1−4] Additionally, the formation mechanisms of inorganic solids are not well understood, hindering the rational discovery of materials with desirable properties. More kinetically controllable processes are needed to enable the formation of new covalent bonds while preserving other bonds in stable intermediate phases, facilitating the discovery of materials with improved properties.[5]

Alternative synthesis methods were developed to address the aforementioned issues. They use low temperatures to increase the predictability of reaction products and stabilize structures that cannot be obtained through high-temperature solid-state reactions.[6−9] Representative examples are highly successful flux synthesis using alkali metal chalcogenides[10,11] and metals,[11−15] hydro-/solvothermal reactions,[16−20] metathesis reactions,[21−24] and the recently developed mixed hydroxide halide fluxes.[9,25] For example, inorganic fluxes melt at lower temperatures and form liquid serving as a reaction medium like organic solvents in molecular synthesis, and frequently participate in reactions. Accordingly, central atoms have a better chance to assemble building blocks that are not available in a high-temperature solid-state synthesis.

The manipulation of inorganic solid structures has been extensively investigated; however, it is a challenging task due to the multitude of potential structures and the materials' stability at low temperatures. Notwithstanding these challenges, there are successful examples of structure manipulation, mainly through kinetically controlled processes such as topotactic reactions involving the intercalation of guest species,[26−29] deintercalation of weakly bound species,[30,31] and replacing atoms or molecules through ion exchange.[32−35] The first two cases have been widely applied for layered oxides and representatively provide the working mechanism of secondary batteries.[36−38] An interesting example is the topochemical conversion of the layered refractory materials of $M_{n+1}AX_n$ (M = early transition metal; A = Al, Si, and X = C, N) and their boride analogues such as M_2AlB_2 (M = Cr, Mn, Fe) and MAlB

Received: April 15, 2023
Published: July 12, 2023

https://doi.org/10.1021/jacs.3c03925
J. Am. Chem. Soc. 2023, 145, 15951−15962

(M = Mo, W), which have been reported to give the class of MXenes.[39−41]

Chalcogenide compounds with discrete molecular structures often dissolve in appropriate polar solvents and can be used as templates to build more complex structures like open frameworks.[42−48] However, there has been little research on manipulating infinitely extended structures at lower temperatures, aside from basic techniques like ion exchange and intercalation/deintercalation, despite the fact that chalcogenides have a rich structural chemistry and are capable of forming Q−Q bonds (where Q represents chalcogen atoms). Notable examples are the transformation of $A_2Bi_4Se_7$ (A = Rb, Cs) and $Cs_3Bi_7Se_{12}$.[49,50] The former undergoes conversion involving the topotactic oxidative coupling of entire rows of terminal Se^{2-} ions to give Se_2^{2-} groups with the expulsion of alkali ions from the crystals upon exposure to ambient air. Consequently, two-dimensional $A_2Bi_4Se_7$ single crystals transform to three-dimensional ABi_4Se_7 single crystals. The latter involves two successive single-crystal to single-crystal oxidative topotactic transformations when soaked in H_2O, namely, two-dimensional $Cs_3Bi_7Se_{12}$ to $Cs_2Bi_7Se_{12}$ to finally three-dimensional $CsBi_7Se_{12}$.

We report a chemical process that occurs at relatively low temperatures, leading to significant changes in the structure and composition of the inorganic solids. This non-topotactic process can be understood and controlled using acid−base chemistry. We studied two model systems, $K_2Sb_8Q_{13}$ and KSb_5Q_8, which have distinct crystal structures made up of complex three-dimensional and two-dimensional frameworks. These structures consist of highly distorted, Sb-centered octahedra consisting of chalcogen atoms, with a charge-compensating spacer of K^+ ions. To disrupt the interaction between the hard Lewis acidic K^+ ions and the soft Lewis basic chalcogen atoms, we soaked the crystals in a hard basic solution of $N_2H_4{\cdot}H_2O$. Based on hard−soft acid−base (HSAB) principle, we expected the extraction of K^+ ions via specific solvation and coordination of hydrazine molecules.[51] This led to the formation of Sb_2Q_3 nanofibers, where the K^+ and Se^{2-} ions were exsolved to restore the charge neutrality in the solids. This is a highly unusual chemical transformation occurring as low as 100 °C under ambient pressure. It involves a structural reconstruction and significant reorganization of the Sb−Se covalent bond network, even though the crystals are not totally dissolved during the reaction process.

Importantly, if $K_2Sb_8Q_{13}$ and KSb_5Q_8 are S/Se solid solutions, the obtained Sb_2Q_3 nanofibers inherit the solid solution nature of the parent bulk crystals. The random distribution of S and Se atoms was directly observed by atomic resolution spherical aberration-corrected scanning transmission electron microscope (Cs-corrected STEM) equipped with an energy dispersive X-ray spectroscopy (EDS). The composition of the nanofibers directly depends on that of the bulk parent crystals, thereby allowing for delicate tunability for the composition and band gap in a wide range from 1.14 to 1.59 eV. Sb_2Q_3 nanofibers can be easily and efficiently produced in large quantities by using a simple bulk reaction process. The band gap of these nanofibers can be adjusted by changing the reaction conditions, such as the level of basicity, S/Se ratio, and the temperature of the reaction. These nanofibers are also highly versatile and could be used in a variety of technical applications, including energy harvesting,[52−54] energy storage,[55,56] and optoelectronics.[54,57−59] Additionally, when Sb_2Q_3 nanofibers are consolidated into pellets and heated using spark plasma sintering, they exhibit increased anisotropy in heat transport with enhanced phonon scattering in the direction parallel to the press direction.

EXPERIMENTAL SECTION

Starting Materials. The following reagents were used as received unless noted otherwise: potassium chunk (99.5%, Aldrich, USA), antimony shot (99.999%, 5N Plus, Canada), selenium shot (99.999%, 5N Plus, Canada), sulfur pieces (99.999%, Alfa Aesar, USA), hydrazine monohydrate (99+%, Alfa Aesar, USA), *N*,*N*-dimethylformamide (DMF, HPLC grade, Samchun, Korea), acetonitrile (HPLC grade, Samchun, Korea), and diethyl ether (99.5%, Samchun, Korea). DMF and acetonitrile were purified in a column of molecular sieves using a Grubbs-type purification system before use.[60] K_2Q (Q = S, Se) was prepared by a stoichiometric reaction of elemental K and Q in liquid NH_3 as described elsewhere.[61] **CAUTION: Hydrazine monohydrate is highly toxic and should be handled using proper protective equipment (gloves, clothing, eye protection) with special care to prevent contact with either the vapors or liquid. Containers may explode when heated. Extreme care should be taken when solvothermal reactions are conducted with hydrazine-containing chemicals. It requires all necessary precautions to ensure safe handling and storage.**

Determination of the Phase Boundary and Synthesis of Parent Crystals of $K_2Sb_8Se_{13-l}S_l$ and $KSb_5Se_mS_{8-m}$ (l = 0, 1.3, 2.6, 3.9; m = 0, 2.0, 4.0, 4.8, 5.5). All the preparations for syntheses were carried out under an argon-filled glovebox (99.999% purity) where the concentration of H_2O and O_2 was kept at less than 1 ppm. An appropriate ratio of K_2Q, Sb, and Q starting reagents was loaded into carbon-coated fused-silica tubes. The total weight of reactants was ∼3 g. The tubes were then evacuated to a pressure of $\sim 10^{-4}$ Torr and subsequently flamed-sealed. The reaction tubes were heated to 850 °C in 12 h and soaked for 5 days, followed by being cooled to room temperature naturally. The products were washed with purified DMF to remove possible residues, followed by drying with ether under an argon flow. For $0 \le l \le 3.9$, the nominal compositions of $K_2Sb_8Se_{13-l}S_l$ gave pure black glossy thick rod-shaped crystals with an ∼100% yield, without releasing any residues when soaked in purified DMF. Typically, these structures exhibit dimensions of approximately 150−250 μm in length and 20 μm in thickness. As the composition's S concentration increases, they tend to become shorter and thicker. For $3.9 < l < 4.1$, products gave a very faint yellow-tinted solution when washed with purified DMF, revealing the mixture of $K_2Sb_8Se_{13}$- and KSb_5S_8-type structures. This observation indicates the removal of a small amount of residual K_2Q_z (Q = S, Se, and Se/S solid solutions; z = 1−6). For $0 \le m \le 5.5$, the nominal compositions of $KSb_5Se_mS_{8-m}$ provided dark red plate crystals with 100% yield. Their lateral dimension is typically ∼100 μm. They grow greater with the higher concentration of Se in the composition.

Synthesis of $Sb_2Se_{3-x}S_x$ Nanofibers under a Solvothermal Condition. Note that the parent crystals can either decompose or not react depending on the concentration of the $N_2H_4{\cdot}H_2O$ solution. The thickness of the nanofiber products is also affected by the concentration of the $N_2H_4{\cdot}H_2O$ solution. The optimized concentration giving the thinnest diameter of products decreases with the increasing mole fraction of S (n_S/n_Q) in the bulk crystals (Table S1). A 0.300 g amount of synthesized parent crystals was dispersed in 16 mL of $N_2H_4{\cdot}H_2O$ solution diluted with deionized water in various volumetric ratios and transferred to 45 mL Teflon-lined stainless steel autoclaves. They were heated at 170−180 °C for 36 h. Products were filtered and washed with purified DMF to remove possible residues in an argon atmosphere, followed by drying in a vacuum at 90 °C for 12 h.

Synthesis of $Sb_2Se_{3-x}S_x$ Nanofibers under an Ambient-Pressure Condition. For control reactions, we conducted the same reaction at 100 °C with magnetic stirring at 200 rpm using a standard Schlenk line technique in an argon atmosphere rather than autoclaves under high temperature and high pressure.

https://doi.org/10.1021/jacs.3c03925
J. Am. Chem. Soc. 2023, 145, 15951−15962

Synthesis of $Sb_2Se_{3-x}S_x$ Control Bulk Powders. Bulk powders of $Sb_2Se_{3-x}S_x$ (x = 0, 1, 2, 2.12, and 3) were synthesized by melting an appropriate molar ratio of elemental starting reagents, such as Sb, S, and Se, in evacuated fused-silica tubes at 650 °C for 12 h. The obtained ingot samples were manually ground with an agate mortar and pestle in an argon-filled glovebox.

Consolidating Powders for Thermal Conductivity Measurements. Powders were loaded in a 13-mm-diameter graphite die in an argon-filled glovebox. After the graphite dies were placed in a spark plasma sintering (SPS) system (SPS-211Lx, Fuji Electronic Industrial, Japan), they were compacted at 400 °C for 5 min under an axial pressure of 50 MPa in a vacuum of ~1.4×10^{-2} Torr using SPS. The relative densities of the samples were ~96% of their theoretical values.

Transmission Electron Microscopy (TEM). $Sb_2Se_{3-x}S_x$ nanofiber samples were investigated by using a JEOL JEM-2100F transmission electron microscope at 200 kV with an Oxford X-Max^N 50TLE EDS detector. For cross-sectional STEM specimens were prepared by focused ion beams (FIB, Helios 650, FEG, FEI). The atomic structures and chemical compositions of specimens were examined using a spherical aberration-corrected JEM-ARM200F microscope (Cold FEG Type, JEOL) equipped with a silicon drift detector (SDD)-type EDS detector (Solid Angle 0.9-sr, X-Max^N 100TLE, Oxford Instruments) at 200 kV installed at the National Center for Interuniversity Research Facilities (NCIRF) at Seoul National University. For high-angle annular dark-field (HAADF) STEM images, the point-to-point resolution was about 80 pm after the spherical aberration correction, and the angular range of the annular detector used was 68−280 mrad. All images were acquired with a high-resolution CCD detector using a 2k × 2k pixel device (UltraScan 1000, Gatan). For STEM-EDS analyses, elemental maps were acquired with a probe size of 0.13 nm and a probe current of 40 pA. The convergence and collection semiangles were 19 and 52 mrad, respectively.

Additional Experimental Details. Further experimental details about analytical techniques can be found in the Supporting Information.

RESULTS AND DISCUSSION

Structure of Sb_2Se_3, $K_2Sb_8Q_{13}$, and KSb_5Q_8 (Q = S, Se, and Their Mixtures). The Sb_2Q_3 structural motif serves as a major building block for many complex chalcogenide compounds with the late group 15 elements of Sb and Bi with the trivalent formal charge as a coordinating center (Figure 1a), showing remarkably rich structural chemistry. The Sb_2Se_3 structure consists of parallel double ribbons of $[Sb_4Se_6]$ units stacked along the crystallographic b-axis via Sb−Se covalent bonds with a distance from 2.588 to 3.007 Å (Figure 1b).[62] Each one-dimensional $[Sb_4Se_6]_n$ ribbon is further weakly bound by the long Sb···Se interaction at 3.215−3.247 and 3.486 Å to form a pseudo-three-dimensional framework.[63] The weakly bound spaces between the ribbons of the framework could theoretically accommodate guest species by breaking Sb−Se bonds and forming derivative structures. However, this has proven to be a difficult and rare feat. This observation suggests that the framework indeed possesses a three-dimensional structure.

$K_2Sb_8Se_{13}$ forms a complex 3D framework consisting of significantly distorted $[SbSe_6]$ octahedra. More descriptively, it can be understood as a modular structure of CdI_2- and NaCl-type building blocks made up of Sb and Se atoms, viewed down the a-axis (Figure 1c).[64] Alternatively, its structure can also be seen as an assembly of one-dimensional $[Sb_4Se_6]$ and $[Sb_4Se_6][SbSe_3]$ chains via sharing Se atoms, running down the same axis, as reflected in the rod-shaped crystal morphology. Charge-balancing K^+ cations fill the resulting one-dimensional channels. Namely, the very hard acidic K^+ cations are surrounded by soft basic Se^{2-} anions in the $[Sb_8Se_{13}]^{2-}$ covalent framework. According to the HSAB principle, hard acids tend to bind to hard bases to attain the thermodynamic stability of the complexes they form.[51,65,66] On that account, we hypothesized that exposing $K_2Sb_8Se_{13}$ to highly hard basic solvents may cause the extraction of the K^+ cations from the framework, forming soluble complexes with the solvent.

KSb_5S_8 crystallizes in a very different structure from Sb_2Se_3 and $K_2Sb_8Se_{13}$. The structure is defined by infinite anionic corrugated layers of $[Sb_5S_8]^-$ composed of distorted $[SbS_6]$ octahedra (Figure 1d).[67−69] Charge-compensating spacer K^+

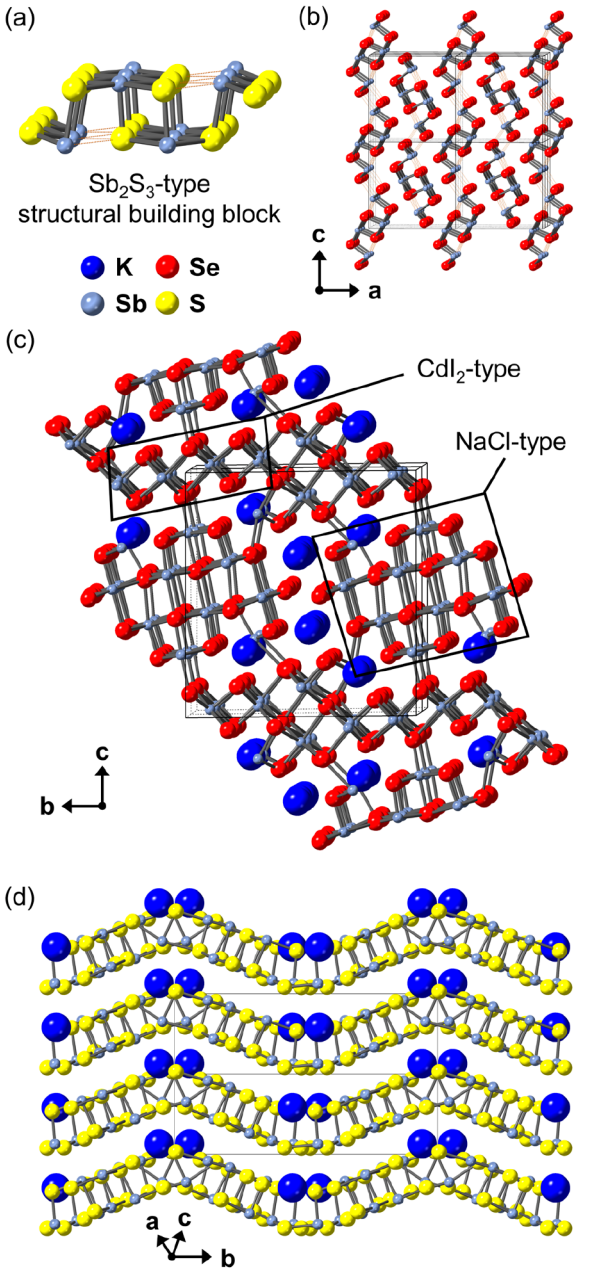

Figure 1. Structures of Sb_2Se_3, $K_2Sb_8Se_{13}$, and KSb_5S_8. (a) Sb_2S_3-type structural building block. Sb_2Q_3 (Q = S, Se, and their mixtures) phases are isostructural. Crystal structure of (b) Sb_2Se_3 down the b-axis, (c) $K_2Sb_8Se_{13}$ down the a-axis, and (d) KSb_5S_8 down the [−101] direction.

https://doi.org/10.1021/jacs.3c03925
J. Am. Chem. Soc. 2023, 145, 15951−15962

cations are located in interlayer spaces via ionic bonds with terminal S atoms in the $[Sb_5S_8]^-$ lattices. Similar to the case of $K_2Sb_8Se_{13}$, highly hard acidic K^+ cations interact with soft basic S^{2-} anions in the $[Sb_5S_8]^-$ layers. Accordingly, HSAB chemistry is expected to transform the KSb_5S_8 compound under proper reaction conditions. For both $K_2Sb_8Se_{13}$ and KSb_5S_8, extracting the K^+ cation by a hard basic solution would be accompanied by leaching the chalcogenide ion Q^{2-} (Q = S, Se) for charge compensation. It turns out hydrazine is an effective solvent to accomplish this task.

Transformation under Solvothermal Conditions. Based on the above hypothesis, $K_2Sb_8Se_{13}$ and KSb_5S_8 bulk crystals were reacted with $N_2H_4{\cdot}H_2O$ in argon-filled Teflon-lined stainless-steel autoclaves at 180 and 170 °C, respectively. Scanning electron microscope (SEM) images show that thick micrometer-sized rods of as-synthesized $K_2Sb_8Se_{13}$ bulk crystals transform to completely dispersed nanofibers with a typical thickness of ∼50 nm and a length of ∼50 μm (Figures 2 and S1a). After washing a possible exsolved residue of K_2Se with purified DMF under an Ar flow, the powder X-ray diffraction (PXRD) pattern of the product matches with the theoretical calculation for the Sb_2Se_3 structure (Figure S2). Elemental analyses using EDS (Figure S1b) and a field emission electron probe microanalyzer (FE-EPMA) (Table 1) indicated compositions close to "Sb_2Se_3" without the presence of any K atoms.

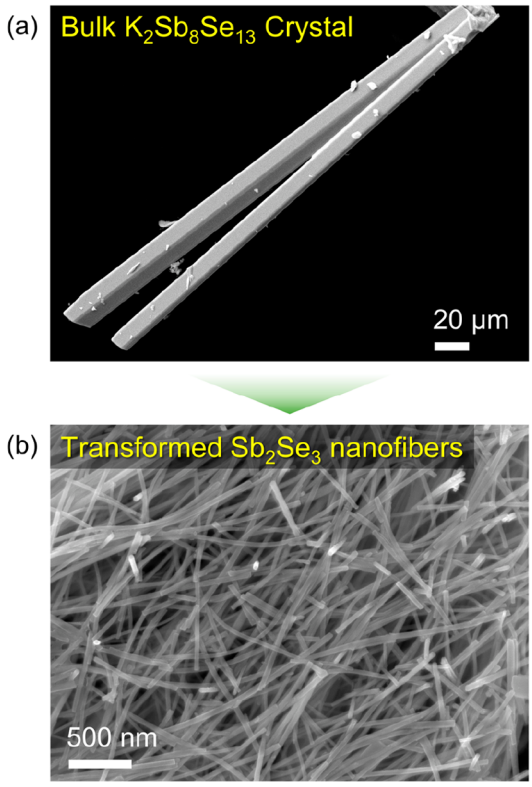

Figure 2. Representative SEM images for (a) as-prepared $K_2Sb_8Se_{13}$ bulk crystals and (b) transformed Sb_2Se_3 nanofibers.

Remarkably, although platelike KSb_5S_8 crystals do not involve any $[Sb_2Se_3]$-related structural motif, they show a solution chemistry similar to the $K_2Sb_8Se_{13}$ case. The products after 36 h are nano/microrods with a typical thickness of ∼100 nm and a length of ∼15 μm (Figure S1a), identified as Sb_2S_3 by the EDS and PXRD analyses (Figures S1b and S2). This result implies that significant structural reorganization occurs by the reaction between KSb_5S_8 crystals and $N_2H_4{\cdot}H_2O$. Consistent with our hypothesis for both $K_2Sb_8Se_{13}$ and KSb_5S_8, K_2Q is dissolved out of the structures by the $N_2H_4{\cdot}H_2O$, and Sb_2Q_3 nano/microfibers evolve.

Table 1. Chemical Compositions of the Products Transformed from the Parent Materials Analyzed by a Field Emission Electron Probe Microanalyzer (FE-EPMA)[a]

parent crystal structure type	parent materials used	n_S/n_Q	average analyzed compositions by FE-EMPA
$K_2Sb_8Se_{13}$	$K_2Sb_8Se_{13}$	0	$Sb_{2.01(1)}Se_{2.99(1)}$
	$K_2Sb_8Se_{11.7}S_{1.3}$	0.10	$Sb_{2.02(1)}Se_{2.87(2)}S_{0.11(1)}$
	$K_2Sb_8Se_{10.4}S_{2.6}$	0.20	$Sb_{2.00(1)}Se_{2.63(2)}S_{0.37(2)}$
	$K_2Sb_8Se_{9.1}S_{3.9}$	0.30	$Sb_{2.00(1)}Se_{2.31(2)}S_{0.69(2)}$
KSb_5S_8	$KSb_5Se_4S_4$	0.50	$Sb_{2.00(1)}Se_{1.72(2)}S_{1.29(2)}$
	$KSb_5Se_2S_6$	0.75	$Sb_{2.01(1)}Se_{0.87(2)}S_{2.12(3)}$
	KSb_5S_8	1	$Sb_{2.00(1)}S_{3.00(2)}$

[a] n_S/n_Q denotes a molar ratio of S atoms to total chalcogen atoms in parent materials. The standard deviation in the average analyzed compositions by FE-EPMA is given in parentheses.

We further investigated if solid solution $Sb_2Se_{3-x}S_x$ nanofibers with x-dependent band gap tunability can be similarly achievable from solid solution phases of the respective solid solution $K_2Sb_8Q_{13}$ and KSb_5Q_8 crystals. Note that the opposite end members $K_2Sb_8S_{13}$ and KSb_5Se_8 do not exist, indicating that the former structure can be stabilized only in Se-rich conditions and vice versa. Hence, we first defined the phase boundary between $K_2Sb_8Se_{13}$- and KSb_5S_8-type structures with respect to the alloying ratio of S and Se atoms by using PXRD (Figures 3 and S3). We performed direct combination reactions for the nominal compositions of "$K_2Sb_8Se_{13-l}S_l$" (l = 0−4.1) and "$KSb_5S_{8-m}Se_m$" (m = 0−5.5) by a solid-state reaction. The products were subsequently washed with purified DMF under an Ar flow to remove possible residual K_2Q_z (Q = S, Se, and Se/S solid solutions; z = 1−6) if present. The PXRD patterns of the former series show that the pure triclinic $K_2Sb_8Se_{13}$-type structure is stabilized in a relatively narrow range of the S concentration, namely, $0 \le l \le 3.9$ in the nominal composition of "$K_2Sb_8Se_{13-l}S_l$". The maximum mole fraction of S to the total chalcogen atoms (n_S/n_Q) is 0.300. When l is equal to or greater than 4.1 ($n_S/n_Q \ge 0.315$), the $K_2Sb_8Se_{13}$-type structure does not form anymore, and instead, KSb_5S_8 structure type solid solutions stabilize (Figure S4). In the intermediate range of $3.9 < l < 4.1$, $K_2Sb_8Se_{13}$ and KSb_5S_8 structure type solid solutions coexist, determining the phase boundary. On the other hand, the PXRD patterns of the latter series present that the monoclinic KSb_5S_8-type structure crystallizes in a broad range of $0 \le m \le 5.5$ in the nominal composition "$KSb_5S_{8-m}Se_m$" (namely, $0.313 \le n_S/n_Q \le 1.0$). The samples with both $K_2Sb_8Se_{13}$- and KSb_5S_8-type structures show the preferred orientation for the (016) and (222) Bragg peaks in the PXRD patterns, respectively. These correspond to the growth direction of the pseudo-one-dimensional chain in the former and the stacking direction perpendicular to the layers in the latter, respectively (Figure S5).[64,67]

After the phase boundary between $K_2Sb_8Se_{13}$- and KSb_5S_8-type structures was confirmed, solid solution bulk crystal precursors of $K_2Sb_8Se_{13-l}S_l$ and $KSb_5S_{8-m}Se_m$ were solvothermally reacted with $N_2H_4{\cdot}H_2O$ solvent as summarized in Table S1. $K_2Sb_8Se_{13-l}S_l$ and $KSb_5S_{8-m}Se_m$ parent materials yield

https://doi.org/10.1021/jacs.3c03925
J. Am. Chem. Soc. 2023, 145, 15951−15962

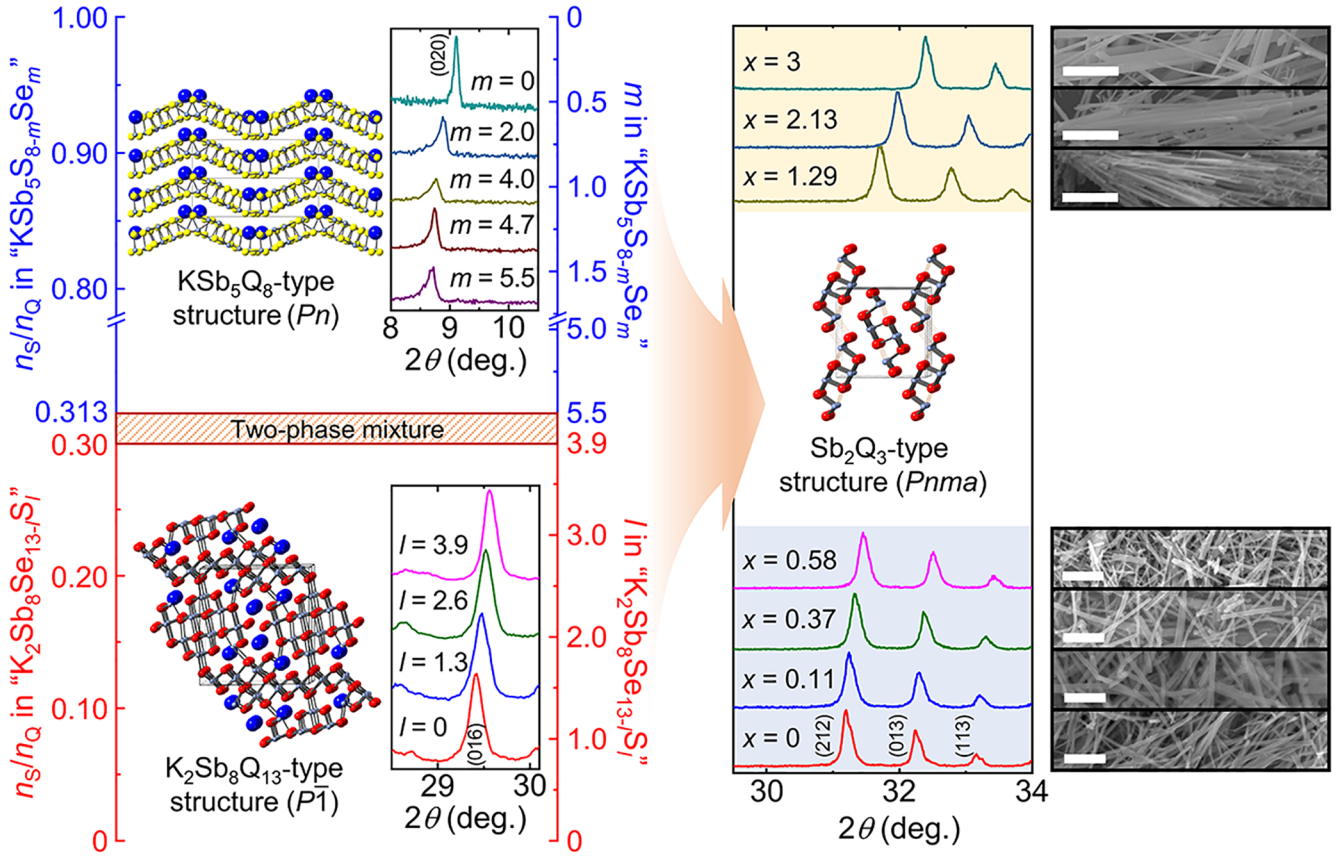

Figure 3. Phase boundary between $K_2Sb_8Q_{13}$- and KSb_5Q_8-type crystal structure (Q = S, Se, and their mixtures) with respect to the relative ratio of S to Q (n_S/n_Q) in the nominal compositions "$K_2Sb_8Se_{13-l}S_l$" and "$KSb_5S_{8-m}Se_m$", determined by their powder XRD patterns. The former structure type stabilizes in Se-rich conditions. At the intermediate range of $0.300 < n_S/n_Q < 0.313$, $K_2Sb_8Q_{13}$- and KSb_5Q_8-type solid solutions coexist. At $n_S/n_Q \geq 0.313$, KSb_5Q_8-type solid solutions exclusively form. A gradual upshift of the characteristic (016) and (020) Bragg peaks for $K_2Sb_8Q_{13}$ and KSb_5Q_8 structures, respectively, is shown in the left panels. Note that both $K_2Sb_8Q_{13}$- and KSb_5Q_8-type solid solutions transform to Sb_2Q_3 nanofibers under the proper reaction conditions, as observed in the corresponding PXRD patterns and SEM images in the right panels. White scale bars correspond to 500 nm.

nanofibrous products with a typical diameter of ~50 nm and a length of ~50 μm for the former and a diameter of ~100 nm and a length of ~15 μm for the latter (Figure 3). Their PXRD patterns are fully indexed to an orthorhombic *Pnma* Sb_2S_3-type structure without secondary phase within the detection limit of a laboratory XRD instrument (Figures 3 and S2). The unit cell dimensions isotropically contract almost linearly with the higher content of smaller S atoms following Vegard's law, implying S and Se atoms are randomly disordered in the anionic sublattice in the nanofibers (Figure 4a and Table S2).

The results of elemental analysis using an electron probe microanalyzer (EPMA) show that the concentration of S in the transformed $Sb_2Se_{3-x}S_x$ nanofibers is finely tunable because it directly depends on that in bulk crystal precursors of $K_2Sb_8Se_{13-l}S_l$ and $KSb_5S_{8-m}Se_m$ (Figure 4b and Table 1). We denote the mole fraction of S to Q in $Sb_2Se_{3-x}S_x$ nanofibers as $n_{S,nano}/n_{Q,nano}$. The $n_{S,nano}/n_{Q,nano}$ is smaller than the corresponding ratio in the starting bulk precursors. For example, the $n_{S,nano}/n_{Q,nano}$ of 0.12 and 0.43 are derived from the bulk parent materials with n_S/n_Q = 0.20 and 0.50, respectively. When a smaller mole fraction of S substitutes for Se in $K_2Sb_8Se_{13-l}S_l$, namely, $n_S/n_Q \leq 0.20$, the $n_{S,nano}/n_{Q,nano}$ in $Sb_2Se_{3-x}S_x$ nanofibers increases parabolically with the increasing S mole fraction in the precursors. For $n_S/n_Q > 0.20$, however, the $n_{S,nano}/n_{Q,nano}$ increases almost linearly with increasing n_S/n_Q in the bulk precursors (Figure 4b). We conducted the solvothermal reaction for the $K_2Sb_8Se_{13}$ bulk crystal under the same conditions with soft basic acetonitrile (CH_3CN). However, we did not observe any structural change (Figure S6). This verifies that the observed transformation is driven by HSAB interaction with the suitably hard basic solution to extract K^+ cations.

Transformation under Ambient Pressure. We also performed control reactions for $K_2Sb_8Se_{13-l}S_l$ and $KSb_5S_{8-m}Se_m$ (l = 0, 3.9; m = 0, 5.5) bulk crystals at 100 °C under ambient pressure rather than a high-temperature and high-pressure solvothermal environment, keeping all the other conditions the same as the previous cases, namely, the concentration and volumetric ratio of the $N_2H_4{\cdot}H_2O$ solution (Table S1). The resulting products were investigated by using SEM and PXRD (Figures S10). Remarkably, the $K_2Sb_8Se_{13}$ (n_S/n_Q = 0) sample transforms to Sb_2Se_3 without the need of solvothermal conditions (Figure S7). Note that the average thickness of the obtained Sb_2Se_3 nanofibers is smaller at ~15 nm compared to ~50 nm for solvothermally transformed fibers. However, the S alloyed $K_2Sb_8Se_{9.1}S_{3.9}$ solid solution sample (l = 3.9 and n_S/n_Q = 0.30) partially converts to $Sb_2Se_{3-x}S_x$ nanofibers with a small fraction of the unreacted

https://doi.org/10.1021/jacs.3c03925
J. Am. Chem. Soc. 2023, 145, 15951−15962

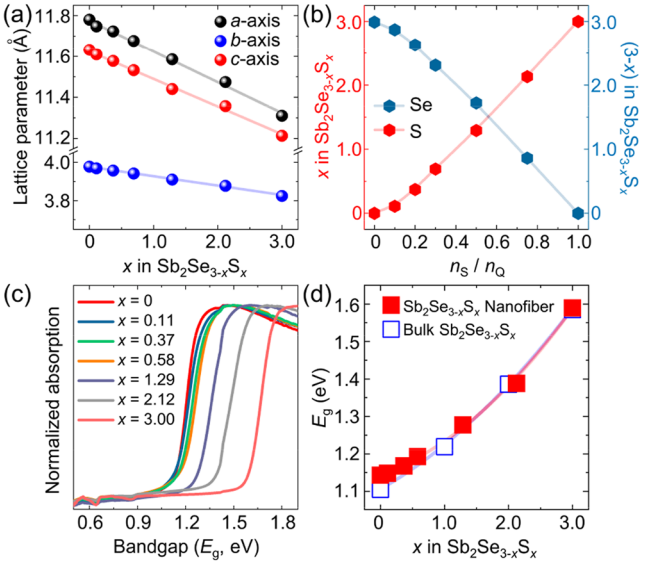

Figure 4. (a) The lattice parameters of transformed $Sb_2Se_{3-x}S_x$ nanofibers with respect to the concentration of S atoms in the composition. (b) The concentration of S and Se atoms in $Sb_2Se_{3-x}S_x$ nanofibers as a function of the mole fraction of S in the parent crystals of $K_2Sb_8Se_{13-l}S_l$ and $KSb_5S_{8-m}Se_m$ precursors (n_S/n_Q). The analyzed compositions were determined by EPMA. (c) Normalized optical absorption spectra of $Sb_2Se_{3-x}S_x$ nanofibers as a function of the S concentration, confirming their band gap tunability. (d) The band gap as a function of the S concentration in $Sb_2Se_{3-x}S_x$ nanofibers in comparison with those of $Sb_2Se_{3-x}S_x$ bulk counterparts prepared by high-temperature solid-state reaction. The observed spectra of the latter are given in Figure S12.

parent material at the same reaction condition (Figure S8). The resultant nanofibers show an average thickness of ~15 nm and a similar analyzed composition of '$Sb_{2.01}Se_{2.29}S_{0.71}$' by EDS to that of solvothermally transformed fibers. The $KSb_5S_{2.5}Se_{5.5}$ sample with the increased fraction of S alloying (n_S/n_Q = 0.313) does not react with the $N_2H_4{\cdot}H_2O$ solution according to the PXRD and EDS results (Figure S9a and S9b). Instead, its bulk crystals physically exfoliate to form nanowires with an average diameter of ~25 nm (Figure S9c). Mechanical exfoliation could not be achieved for the pure sulfide KSb_5S_8 (n_S/n_Q = 1) sample (Figure S10).

These observations imply that the transformative reaction by $N_2H_4{\cdot}H_2O$ solution is directly affected by the n_S/n_Q ratio in the reactant bulk crystals and reaction conditions such as the pressure and concentration of solvents driving HSAB reactions. As the fraction of the harder Lewis basic S^{2-} in the parent crystals increases, the driving force to form the hard acid–hard base adduct $[K(N_2H_4)_x]^+$ decreases. Note that variations of both the hardness of the cations and the softness of the anions are important in this chemistry given the complete reactions. Under the relatively high pressure present in solvothermal conditions, the HSAB reaction accelerates, favoring the growth of thicker fibers. Consequently, structural and chemical transformations driven by HSAB interactions can be delicately tunable by controlling the reaction conditions.

Optical Band Gap Tunability. The solid-state optical absorption spectra of the obtained $Sb_2Se_{3-x}S_x$ nanofibers reveal that their absorption edge shifts gradually from 1.14 eV for Sb_2Se_3 to 1.59 eV for Sb_2S_3 (Figure 4c), confirming their fine optical band gap (E_g) tunability over a wide near-infrared spectral range. This observation implies that Se and S atoms are randomly distributed to form solid solution $Sb_2Se_{3-x}S_x$ nanofibers in contrast to typical phase segregations found in $Sb_2Se_{3-x}S_x$ nanomaterials prepared by conventional bottom-up synthesis methods.[70,71] The measured E_g values can be fitted as a function of the S concentration, x, by a standard bowing equation:[72]

$$E_g(x) = P_1(1 - x/3) + P_2(x/3) - B(x/3)(1 - x/3)$$

where P_1 and P_2 are E_g at x = 0 and 3, respectively, and B is the bowing parameter, whose value is ~0.27 eV, showing the quadratic increase with the higher S mole fraction in the $Sb_2Se_{3-x}S_x$ nanofibers. They are comparable to those for the bulk counterparts (Figures 4d and S11) due to their macroscopic dimension along the fiber growth direction. The controllability of E_g in $Sb_2Se_{3-x}S_x$ nanofibers, coupled with their inherent high absorption coefficients,[73,74] plays a crucial role in various optoelectronic applications. These applications include photodetection[57,75,76] and solar light harvesting, where the ability to manipulate the band gap enables enhanced performance and efficiency.[52,63,77−80]

Direct Observation of Atomic Arrangement. According to the laboratory PXRD patterns, superior thermoelectric systems of $AgPb_mSbTe_{2+m}$ (LAST-m; $[AgSbTe_2][PbTe]_m$)[81] and $Sn_{1-x}Pb_xSe$ ($[SnSe]_{1-x}[PbSe]_x$)[82−85] follow Vegard's law with respect to the ratio of two end members. Accordingly, they have been believed to form solid solutions. However, the TEM studies have revealed that a substantial degree of nanostructures with a compositional fluctuation is embedded in the surrounding matrix in these materials.[82,86,87] The importance of atomic-resolution analysis to properly confirm the solid solution nature is highlighted by these observations. Nanostructures have unique interactions with charge carriers and phonons, which greatly impact the electrical and thermal properties of the bulk materials.[82,88−94]

Representative low-magnification TEM images of the Sb_2Se_3 nanofibers transformed from $K_2Sb_8Se_{13}$ bulk crystals show a single-crystalline nanofibrous morphology (Figure 5a). The corresponding fast Fourier transform (FFT) image shows a single set of the diffraction spots down the [10−1] zone axis of the Sb_2Se_3 structure and the growth direction of the nanofibers along the [010] direction (inset of Figure 5a). The magnified image taken at the red rectangular region in Figure 5a clearly displays periodic spacings of ~0.831 and ~0.398 nm between the repeating atomic arrays, corresponding to the interval of the (101) and (010) planes, respectively (Figure 5b). Indeed, the observed atomic arrangement coincides with the Sb_2Se_3 structure viewed down the same zone axis. Similar results are observed for "$Sb_2Se_{1.72}S_{1.29}$" (analyzed composition by FE-EPMA) nanofibers (Figure 5c). The repeating interval distance along the [101] and [010] directions is reduced to ~0.814 and ~0.391 nm, respectively, along the [10−1] zone axis due to the substitution of smaller S atoms for Se atoms (Figure 5d). All constituent elements are homogeneously distributed over the Sb_2Se_3 and $Sb_2Se_{1.72}S_{1.29}$ nanofibers at the resolution of TEM and the corresponding EDS elemental analysis (Figure S12).

To directly determine the location of the constituent elements in the $Sb_2Se_{1.72}S_{1.29}$ nanofibers, we took HAADF images using Cs-STEM. Figure 5e clearly reveals the atomic arrangement of zigzag $[Sb_4Q_6]_n$ double-ribbon building blocks viewed down the [010] zone axis and the van der Waals gap between them. Because the signal intensity of the HAADF-STEM image is approximately proportional to the square of the atomic number, bigger and brighter spheres can be

https://doi.org/10.1021/jacs.3c03925
J. Am. Chem. Soc. 2023, 145, 15951−15962

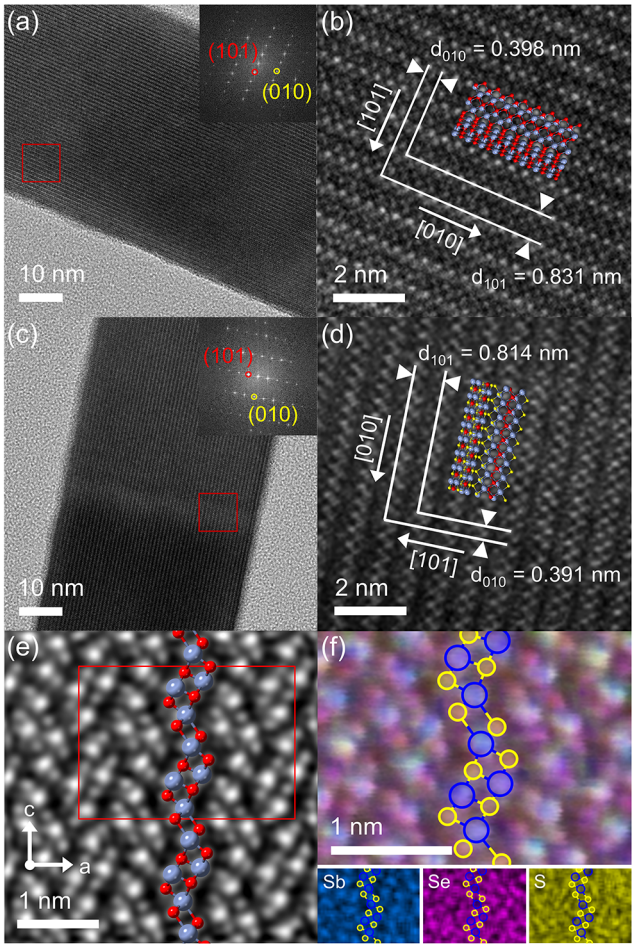

Figure 5. (a) Typical low-magnification TEM and the corresponding FFT image down the [10−1] zone axis (inset) of the transformed Sb_2Se_3 nanofiber sample, showing its single-crystal nature and the growth direction along the [010] direction. The selected spots in the FFT image are indexed. (b) High-resolution TEM image taken at the red rectangular region in (a). The (101) and (010) lattice planes are indexed. (c) Typical low-magnification TEM and the corresponding FFT image down the [10−1] zone axis (inset) of the transformed "$Sb_2Se_{1.72}S_{1.29}$" nanofiber sample, showing its single-crystal nature and the growth direction. (d) Enlarged TEM image obtained at the red rectangular region in (c). The (101) and (010) lattice planes are indexed. (e) Atomic-resolution HAADF-STEM image of the transformed "$Sb_2Se_{1.72}S_{1.29}$" nanofiber sample along the [010] zone axis. (f) Atomic-resolution elemental maps of Sb, Se, and S atoms by STEM-EDS recorded at the red rectangular region in (e) (upper panels). It is created by overlaying respective EDS signals from Sb, Se, and S atoms displayed in blue, magenta, and yellow, respectively (lower panel). Sb_2Se_3 structure is overlaid on (b), (d), (e), and (f) for comparison. "$Sb_2Se_{1.72}S_{1.29}$" and "$Sb_2Se_{1.72}S_{1.29}$" are the analyzed composition by EPMA.

assigned to the ^{51}Sb atom unambiguously and smaller and fainter ones to the ^{34}Se or ^{16}S atom. We recorded atomic-resolution elemental maps using STEM-EDS in the red rectangular area in Figure 5e to directly observe elemental arrangements in the nanofibers. The top panel in Figure 5f is the overlay of the respective EDS signals directly from the constituent Sb, Se, and S atoms shown in the lower panel. These results confirm that Se and S atoms are randomly distributed at the anion sites in the Sb_2S_3-type structure, and our transformed $Sb_2Se_{3-x}S_x$ nanofibers crystallize in solid solutions.

Enhanced Anisotropy in Thermal Conductivity. The obtained Sb_2Se_3 nanofibers were consolidated into a dense bulk pellet (>∼96% of the theoretical density) by SPS. We similarly prepared a control SPS sample of bulk Sb_2Se_3 powders synthesized by a high-temperature solid-state reaction. Because of the one-dimensional crystal structure of Sb_2Se_3, the PXRD patterns for both pellets show significant preferred orientation perpendicular to the pressing direction of SPS (Figures 6a and S13). The contrasting morphologies of

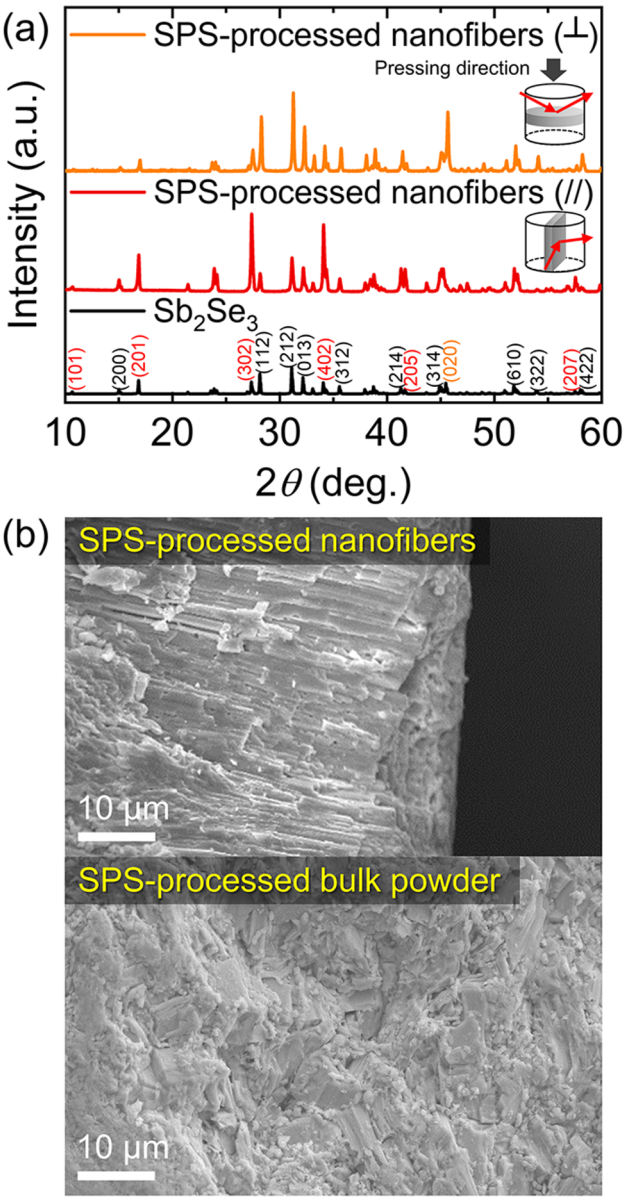

Figure 6. (a) The PXRD patterns of the SPS-processed Sb_2Se_3 nanofibers taken perpendicular (⊥; upper, orange) and parallel (||; middle, red) to the pressing direction in comparison with the theoretical calculation for Sb_2Se_3 (ICDD PDF No. 75-1462). The selected peaks are indexed. (b) Representative cross-sectional SEM images of the SPS-processed pellet samples of the transformed Sb_2Se_3 nanofibers (upper) and melt-synthesized bulk powders. Highly oriented nanofibrous morphology is evident in the former, in sharp contrast to the irregular feature in the latter.

https://doi.org/10.1021/jacs.3c03925
J. Am. Chem. Soc. 2023, 145, 15951−15962

the two pellets are clearly depicted in representative cross-sectional SEM images. The title sample exhibits a remarkable well-oriented, fibrous morphology, while the control sample displays randomly oriented, irregular grains. This difference in morphology is visually striking, as shown in Figure 6b.

We also performed temperature-dependent total thermal conductivity (κ_{tot}) measurements along the perpendicular ($\kappa_{tot,\perp}$) and parallel ($\kappa_{tot,\parallel}$) pressing SPS directions. The κ_{tot} for all samples decreases with increasing temperature from room temperature to 200 °C (Figure 7). Remarkably, the title

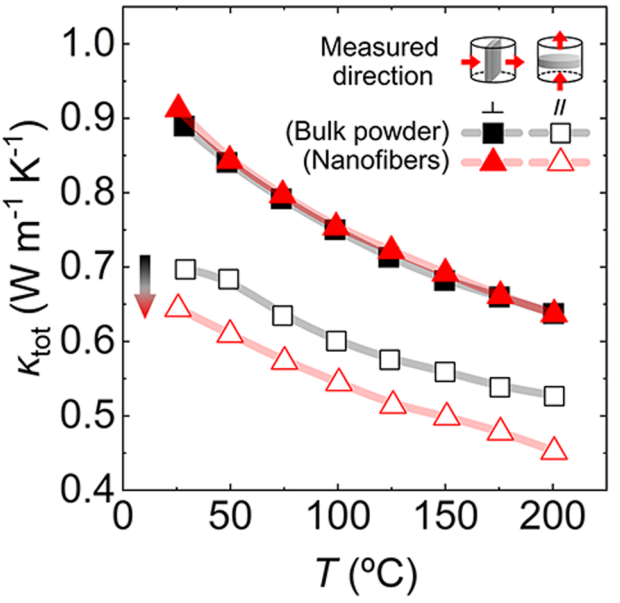

Figure 7. Temperature-dependent total thermal conductivities of the SPS-processed Sb_2Se_3 nanofibers recorded perpendicular (solid) and parallel (open) to the pressing direction in comparison with those of melt-synthesized bulk Sb_2Se_3 powders.

SPS sample exhibits much lower $\kappa_{tot,\parallel}$ than the control samples, while both samples show nearly the same $\kappa_{tot,\perp}$. For example, the $\kappa_{tot,\parallel}$ for the former is ~0.64 and ~0.45 W m^{-1} K^{-1} at 27 and 200 °C, respectively, in comparison with ~0.70 and ~0.52 W m^{-1} K^{-1} for the latter at the same temperature. The significantly increased anisotropy in thermal conductivity in the title pellet is mainly ascribed to the increased phonon scattering at the grain boundaries arising from the nanofibrous morphology.[87] The $\kappa_{tot,\parallel}$ has not been previously reported for any forms of bulk Sb_2Se_3 samples including single crystals and pressed pellets of nanowires to the best of our knowledge. The title sample shows similar $\kappa_{tot,\perp}$ to the reported values for SPS-processed polycrystalline bulk samples at room temperature.[95,96] The κ_{tot} of the individual nanowires and nanotubes ranges from ~0.037 to 1.8 W m^{-1} K^{-1} near room temperature.[71,97,98] Their anisotropy in the κ_{tot} has not been reported.

CONCLUSION

We have demonstrated that the hard–soft acid–base principle can enable us to selectively manipulate crystal structures of inorganic solids via solution chemistry. Hard basic aqueous hydrazine interacts with hard acidic K^+ cations in the inorganic framework and facilitates the breakdown of crystal structures in solid-state materials, leading to the formation of novel morphologies. This chemical process occurs at low temperatures and ambient pressure and drives significant structural reconstruction in insoluble structures such as $K_2Sb_8Se_{13}$ and KSb_5S_8, which involves the complete exsolution of hard basic K^+ cations out of the soft acidic chalcogenide surface of the anionic $[Sb_8Se_{13}]^{2-}$ and $[Sb_5S_8]^-$ lattices. Our findings suggest that solid structures can be manipulated in solution without the need for high temperatures or pressures. The whole process can be elucidated by the hard–soft acid–base principle. This points to effective paths for the delicate design of new structural motifs, compositions, and morphologies. Future work will focus on in situ observation of these transformation processes to uncover the formation mechanism of these and related inorganic solids.

ASSOCIATED CONTENT

Supporting Information

The Supporting Information is available free of charge at https://pubs.acs.org/doi/10.1021/jacs.3c03925.

Additional experimental details about analytical techniques, the optimized volumetric ratio of $N_2H_4{\cdot}H_2O$ solution according to bulk crystals, cell parameters, analyzed compositions, structural motif and crystal structure, SEM-EDS images and corresponding spectra, powder XRD patterns, UV–vis absorption spectra, and TEM-EDS images (PDF)

AUTHOR INFORMATION

Corresponding Authors

In Chung − *School of Chemical and Biological Engineering, and Institute of Chemical Processes, Seoul National University, Seoul 08826, Republic of Korea; Center for Correlated Electron Systems, Institute for Basic Science (IBS), Seoul 08826, Republic of Korea;* orcid.org/0000-0001-6274-3369; Email: inchung@snu.ac.kr

Mercouri G. Kanatzidis − *Department of Chemistry, Northwestern University, Evanston, Illinois 60208, United States;* orcid.org/0000-0003-2037-4168; Email: m-kanatzidis@northwestern.edu

Myung-Gil Kim − *School of Advanced Materials Science & Engineering, Sungkyunkwan University, Suwon 16419, Republic of Korea;* orcid.org/0000-0002-8607-5972; Email: myunggil@skku.edu

Authors

Hyungseok Lee − *School of Chemical and Biological Engineering, and Institute of Chemical Processes, Seoul National University, Seoul 08826, Republic of Korea; Center for Correlated Electron Systems, Institute for Basic Science (IBS), Seoul 08826, Republic of Korea;* orcid.org/0000-0001-6432-5670

Byeongjun Yoo − *School of Chemical and Biological Engineering, and Institute of Chemical Processes, Seoul National University, Seoul 08826, Republic of Korea; Center for Nanoparticle Research, Institute for Basic Science (IBS), Seoul 08826, Republic of Korea*

Dawoon Kim − *School of Chemical and Biological Engineering, and Institute of Chemical Processes, Seoul National University, Seoul 08826, Republic of Korea; Center for Correlated Electron Systems, Institute for Basic Science (IBS), Seoul 08826, Republic of Korea*

Joonil Cha − *School of Chemical and Biological Engineering, and Institute of Chemical Processes, Seoul National University, Seoul 08826, Republic of Korea; Center for Correlated Electron Systems, Institute for Basic Science (IBS), Seoul 08826, Republic of Korea*

Yeo Kyung Kang − *School of Advanced Materials Science & Engineering, Sungkyunkwan University, Suwon 16419, Republic of Korea*

Sung-Pyo Cho − *National Center for Inter-University Research Facilities, Seoul National University, Seoul 08826, Republic of Korea*

Taeghwan Hyeon − *School of Chemical and Biological Engineering, and Institute of Chemical Processes, Seoul National University, Seoul 08826, Republic of Korea; Center for Nanoparticle Research, Institute for Basic Science (IBS), Seoul 08826, Republic of Korea;* orcid.org/0000-0001-5959-6257

Complete contact information is available at: https://pubs.acs.org/10.1021/jacs.3c03925

Notes

The authors declare no competing financial interest.

■ ACKNOWLEDGMENTS

This work was supported by the National Research Foundation of Korea (NRF) grant funded by the Korean government (MSIT) (NRF-2020R1A2C2011111 to I.C. and 2021M3H4A1A02055684 to M.-G.K.) and Institute for Basic Science (IBS-R009-G2). H.L. was partly supported by the Basic Science Research Program through the National Research Foundation of Korea (NRF) funded by the Ministry of Education (RS-2023-00244470). At Northwestern the work was partly supported by the National Science Foundation through grant DMR-2003476.

■ REFERENCES

(1) Kanatzidis, M. G.; Poeppelmeier, K. R.; Bobev, S.; Guloy, A. M.; Hwu, S.-J.; Lachgar, A.; Latturner, S. E.; Raymond; Schaak, E.; Seo, D.-K.; Sevov, S. C.; Stein, A.; Dabrowski, B.; Greedan, J. E.; Greenblatt, M.; Grey, C. P.; Jacobson, A. J.; Keszler, D. A.; Li, J.; Subramanian, M. A.; Xia, Y.; Cagin, T.; Häussermann, U.; Hughbanks, T.; Mahanti, S. D.; Morgan, D.; Seo, D.-K.; Spaldin, N. A.; Buhro, W. E.; Giammar, D. E.; Hollingsworth, J. A.; Johnson, D. C.; Nozik, A. J.; Peng, X.; Bedard, R. L.; Brese, N. E.; Cao, G.; Dhingra, S. S.; Kagan, C. R.; Mitzi, D. B.; Geselbracht, M. J.; Lisensky, G. C.; Lufaso, M. W.; Maggard, P. A.; Michael, O. K.; Wilkinson, A. P.; zur Loye, H.-C.; Egami, T.; Greedan, J. E.; Hodges, J. P.; Martin, J. D.; Parise, J. B.; Toby, B. H.; Vanderah, T. A.; Burns, P. C.; Chan, J. Y.; Meyer, A. E.; Murray, C. B.; Ramirez, A. P.; Ward, M. D.; Yu, L.; Alario-Franco, M. A.; Battle, P. D.; Bein, T.; Cahill, C. L.; Halasyamani, P. S.; Maignan, A.; Seshadri, R. Report from the third workshop on future directions of solid-state chemistry: The status of Solid-State Chemistry and Its Impact in the Physical Sciences. *Prog. Solid State Chem.* **2008**, *36*, 1−133.

(2) Stein, A.; Keller, S. W.; Mallouk, T. E. Turning down the Heat: Design and Mechanism in Solid-State Synthesis. *Science* **1993**, *259*, 1558−1564.

(3) Mrotzek, A.; Kanatzidis, M. G. "Design" in Solid-State Chemistry Based on Phase Homologies. The Concept of Structural Evolution and the New Megaseries $A_m[M_{1+l}Se_{2+l}]_{2m}[M_{2l+n}Se_{2+3l+n}]$. *Acc. Chem. Res.* **2003**, *36*, 111−119.

(4) Kanatzidis, M. G. Structural Evolution and Phase Homologies for "Design" and Prediction of Solid-State Compounds. *Acc. Chem. Res.* **2005**, *38*, 359−368.

(5) Corey, E. J. The Logic of Chemical Synthesis: Multistep Synthesis of Complex Carbogenic Molecules (Nobel Lecture). *Angew. Chem., Int. Ed.* **1991**, *30*, 455−465.

(6) Buck, M. R.; Schaak, R. E. Emerging Strategies for the Total Synthesis of Inorganic Nanostructures. *Angew. Chem., Int. Ed.* **2013**, *52*, 6154−6178.

(7) Uppuluri, R.; Sen Gupta, A.; Rosas, A. S.; Mallouk, T. E. Soft Chemistry of Ion-Exchangeable Layered Metal Oxides. *Chem. Soc. Rev.* **2018**, *47*, 2401−2430.

(8) Chamorro, J. R.; McQueen, T. M. Progress toward Solid State Synthesis by Design. *Acc. Chem. Res.* **2018**, *51*, 2918−2925.

(9) Zhou, X.; Kolluru, V. S. C.; Xu, W.; Wang, L.; Chang, T.; Chen, Y.-S.; Yu, L.; Wen, J.; Chan, M. K. Y.; Chung, D. Y.; Kanatzidis, M. G. Discovery of Chalcogenides Structures and Compositions Using Mixed Fluxes. *Nature* **2022**, *612*, 72−77.

(10) Kanatzidis, M. G. Molten Alkali-Metal Polychalcogenides as Reagents and Solvents for the Synthesis of New Chalcogenide Materials. *Chem. Mater.* **1990**, *2*, 353−363.

(11) Kanatzidis, M. G. Discovery-Synthesis, Design, and Prediction of Chalcogenide Phases. *Inorg. Chem.* **2017**, *56*, 3158−3173.

(12) Kanatzidis, M. G.; Pöttgen, R.; Jeitschko, W. The Metal Flux: A Preparative Tool for the Exploration of Intermetallic Compounds. *Angew. Chem., Int. Ed.* **2005**, *44*, 6996−7023.

(13) Latturner, S. E. Clusters, Assemble: Growth of Intermetallic Compounds from Metal Flux Reactions. *Acc. Chem. Res.* **2018**, *51*, 40−48.

(14) Dickman, M. J.; Latturner, S. E. Metal Nitrides Grown from Ca/Li Flux: $Ca_6Te_3N_2$ and New Nitridoferrate(I) Ca_6 (Li_xFe_{1-x}) Te_2N_3. *J. Am. Chem. Soc.* **2016**, *138*, 10636−10644.

(15) Schmitt, D. C.; Drake, B. L.; McCandless, G. T.; Chan, J. Y. Targeted Crystal Growth of Rare Earth Intermetallics with Synergistic Magnetic and Electrical Properties: Structural Complexity to Simplicity. *Acc. Chem. Res.* **2015**, *48*, 612−618.

(16) Darr, J. A.; Zhang, J.; Makwana, N. M.; Weng, X. Continuous Hydrothermal Synthesis of Inorganic Nanoparticles: Applications and Future Directions. *Chem. Rev.* **2017**, *117*, 11125−11238.

(17) Xiong, W.-W.; Zhang, G.; Zhang, Q. New Strategies to Prepare Crystalline Chalcogenides. *Inorg. Chem. Front.* **2014**, *1*, 292−301.

(18) Xiong, W.-W.; Zhang, Q. Surfactants as Promising Media for the Preparation of Crystalline Inorganic Materials. *Angew. Chem., Int. Ed.* **2015**, *54*, 11616−11623.

(19) Xiong, W.-W.; Athresh, E. U.; Ng, Y. T.; Ding, J.; Wu, T.; Zhang, Q. Growing Crystalline Chalcogenidoarsenates in Surfactants: From Zero-Dimensional Cluster to Three-Dimensional Framework. *J. Am. Chem. Soc.* **2013**, *135*, 1256−1259.

(20) Li, X.; Do, T. T. H.; Granados del Águila, A.; Huang, Y.; Chen, W.; Li, Y.; Ganguly, R.; Morris, S.; Xiong, Q.; Li, D.-S.; Zhang, Q. Two-Dimensional and Emission-Tunable: An Unusual Perovskite Constructed from Lindqvist-Type $[Pb_6Br_{19}]^{7-}$ Nanoclusters. *Inorg. Chem.* **2018**, *57*, 14035−14038.

(21) Martinolich, A. J.; Neilson, J. R. Toward Reaction-by-Design: Achieving Kinetic Control of Solid State Chemistry with Metathesis. *Chem. Mater.* **2017**, *29*, 479−489.

(22) Martinolich, A. J.; Kurzman, J. A.; Neilson, J. R. Polymorph Selectivity of Superconducting $CuSe_2$ Through Kinetic Control of Solid-State Metathesis. *J. Am. Chem. Soc.* **2015**, *137*, 3827−3833.

(23) Todd, P. K.; Neilson, J. R. Selective Formation of Yttrium Manganese Oxides through Kinetically Competent Assisted Metathesis Reactions. *J. Am. Chem. Soc.* **2019**, *141*, 1191−1195.

(24) Ha, T. D. C.; Lee, H.; Kang, Y. K.; Ahn, K.; Jin, H. M.; Chung, I.; Kang, B.; Oh, Y.; Kim, M.-G. Multiscale Structural Control of Thiostannate Chalcogels with Two-Dimensional Crystalline Constituents. *Nat. Commun.* **2022**, *13*, 7876.

(25) Zhou, X.; Malliakas, C. D.; Yakovenko, A. A.; Wilfong, B.; Wang, S. G.; Chen, Y.-S.; Yu, L.; Wen, J.; Balasubramanian, M.; Wang, H.-H.; Chung, D. Y.; Kanatzidis, M. G. Coherent Approach to Two-Dimensional Heterolayered Oxychalcogenides Using Molten Hydroxides. *Nat. Synth.* **2022**, *1*, 729−737.

(26) Lu, W.; Lee, H.; Cha, J.; Zhang, J.; Chung, I. Electronic Structure Manipulation of the Mott Insulator $RuCl_3$ via Single-Crystal to Single-Crystal Topotactic Transformation. *Angew. Chem., Int. Ed.* **2023**, *62*, No. e202219344.
(27) Kwon, N. H.; Jin, X.; Kim, S.-J.; Kim, H.; Hwang, S.-J. Multilayer Conductive Hybrid Nanosheets as Versatile Hybridization Matrices for Optimizing the Defect Structure, Structural Ordering, and Energy-Functionality of Nanostructured Materials. *Adv. Sci.* **2022**, *9*, 2103042.
(28) Gu, T.-H.; Kwon, N. H.; Lee, K.-G.; Jin, X.; Hwang, S.-J. 2D Inorganic Nanosheets as Versatile Building Blocks for Hybrid Electrode Materials for Supercapacitor. *Coord. Chem. Rev.* **2020**, *421*, 213439.
(29) Jin, X.; Gu, T.-H.; Lee, K.-G.; Kim, M. J.; Islam, M. S.; Hwang, S.-J. Unique Advantages of 2D Inorganic Nanosheets in Exploring High-Performance Electrocatalysts: Synthesis, Application, and Perspective. *Coord. Chem. Rev.* **2020**, *415*, 213280.
(30) Zhou, X.; Wilfong, B.; Vivanco, H.; Paglione, J.; Brown, C. M.; Rodriguez, E. E. Metastable Layered Cobalt Chalcogenides from Topochemical Deintercalation. *J. Am. Chem. Soc.* **2016**, *138*, 16432−16442.
(31) Jin, X.; Gu, T.-H.; Kwon, N. H.; Hwang, S.-J. Synergetic Advantages of Atomically Coupled 2D Inorganic and Graphene Nanosheets as Versatile Building Blocks for Diverse Functional Nanohybrids. *Adv. Mater.* **2021**, *33*, 2005922.
(32) Manos, M. J.; Kanatzidis, M. G. Layered Metal Sulfides Capture Uranium from Seawater. *J. Am. Chem. Soc.* **2012**, *134*, 16441−16446.
(33) Feng, M.-L.; Sarma, D.; Gao, Y.-J.; Qi, X.-H.; Li, W.-A.; Huang, X.-Y.; Kanatzidis, M. G. Efficient Removal of $[UO_2]^{2+}$, Cs^+, and Sr^{2+} Ions by Radiation-Resistant Gallium Thioantimonates. *J. Am. Chem. Soc.* **2018**, *140*, 11133−11140.
(34) Wang, R.; Chen, H.; Xiao, Y.; Hadar, I.; Bu, K.; Zhang, X.; Pan, J.; Gu, Y.; Guo, Z.; Huang, F.; Kanatzidis, M. G. $K_x[Bi_{4-x}Mn_xS_6]$, Design of a Highly Selective Ion Exchange Material and Direct Gap 2D Semiconductor. *J. Am. Chem. Soc.* **2019**, *141*, 16903−16914.
(35) Gao, Y.-J.; Sun, H.-Y.; Li, J.-L.; Qi, X.-H.; Du, K.-Z.; Liao, Y.-Y.; Huang, X.-Y.; Feng, M.-L.; Kanatzidis, M. G. Selective Capture of Ba^{2+}, Ni^{2+}, and Co^{2+} by a Robust Layered Metal Sulfide. *Chem. Mater.* **2020**, *32*, 1957−1963.
(36) Jin, X.; Agyeman, D. A.; Kim, S.; Kim, Y. H.; Kim, M. G.; Kang, Y.-M.; Hwang, S.-J. Crucial Roles of Interfacial Coupling and Oxygen Defect in Multifunctional 2D Inorganic Nanosheets. *Nano Energy* **2020**, *67*, 104192.
(37) Jin, X.; Lee, T.; Tamakloe, W.; Patil, S. B.; Soon, A.; Kang, Y.-M.; Hwang, S.-J. In Situ Defect Engineering Route to Optimize the Cationic Redox Activity of Layered Double Hydroxide Nanosheet via Strong Electronic Coupling with Holey Substrate. *Adv. Sci.* **2022**, *9*, 2103368.
(38) Jeon, B.; Kwak, H. H.; Hong, S.-T. Bilayered $Ca_{0.28}V_2O_5{\cdot}H_2O$: High-Capacity Cathode Material for Rechargeable Ca-Ion Batteries and Its Charge Storage Mechanism. *Chem. Mater.* **2022**, *34*, 1491−1498.
(39) Alameda, L. T.; Moradifar, P.; Metzger, Z. P.; Alem, N.; Schaak, R. E. Topochemical Deintercalation of Al from MoAlB: Stepwise Etching Pathway, Layered Intergrowth Structures, and Two-Dimensional MBene. *J. Am. Chem. Soc.* **2018**, *140*, 8833−8840.
(40) Alameda, L. T.; Lord, R. W.; Barr, J. A.; Moradifar, P.; Metzger, Z. P.; Steimle, B. C.; Holder, C. F.; Alem, N.; Sinnott, S. B.; Schaak, R. E. Multi-Step Topochemical Pathway to Metastable Mo_2AlB_2 and Related Two-Dimensional Nanosheet Heterostructures. *J. Am. Chem. Soc.* **2019**, *141*, 10852−10861.
(41) Gogotsi, Y.; Anasori, B. The Rise of MXenes. *ACS Nano* **2019**, *13*, 8491−8494.
(42) Dhingra, S.; Kanatzidis, M. G. Open Framework Structures Based on Se_x^{2-} Fragments: Synthesis of $(Ph_4P)[M(Se_6)_2]$ (M = Ga, In, TI) in Molten $(Ph_4P)_2Se_x$. *Science* **1992**, *258*, 1769−1772.
(43) Bowes, C. L.; Ozin, G. A. Self-Assembling Frameworks: Beyond microporous oxides. *Adv. Mater.* **1996**, *8*, 13−28.
(44) Hanko, J. A.; Kanatzidis, M. G. A Three-Dimensional Framework with Accessible Nanopores: $RbCuSb_2Se_4{\cdot}H_2O$. *Angew. Chem., Int. Ed.* **1998**, *37*, 342−344.
(45) Trikalitis, P. N.; Rangan, K. K.; Bakas, T.; Kanatzidis, M. G. Varied pore organization in mesostructured semiconductors based on the $[SnSe_4]^{4-}$ anion. *Nature* **2001**, *410*, 671−675.
(46) Manos, M. J.; Iyer, R. G.; Quarez, E.; Liao, J. H.; Kanatzidis, M. G. $\{Sn[Zn_4Sn_4S_{17}]\}^{6-}$: A Robust Open Framework Based on Metal-Linked Penta-Supertetrahedral $[Zn_4Sn_4S_{17}]^{10-}$ Clusters with Ion-Exchange Properties. *Angew. Chem., Int. Ed.* **2005**, *44*, 3552−3555.
(47) Kanatzidis, M. G. Beyond Silica: Nonoxidic Mesostructured Materials. *Adv. Mater.* **2007**, *19*, 1165−1181.
(48) Ding, N.; Kanatzidis, M. G. Selective Incarceration of Caesium ions by Venus Flytrap Action of a Flexible Framework Sulfide. *Nat. Chem.* **2010**, *2*, 187−191.
(49) Iordanidis, L.; Kanatzidis, M. G. Redox-Induced "Zipper" Action in $Rb_2Bi_4Se_7$ and $Cs_2Bi_4Se_7$: Coupling of Slabs to a Three-Dimensional Framework through Single-Crystal to Single-Crystal Conversion. *Angew. Chem., Int. Ed.* **2000**, *39*, 1927−1930.
(50) Iordanidis, L.; Kanatzidis, M. G. Redox-Induced "Zipper" Action in the Solid State. Unprecedented Single-Crystal to Single-Crystal to Single-Crystal Cascade Conversions in $Cs_3Bi_7Se_{12}$. Framework Evolution from 2D to 2D′ to 3D. *J. Am. Chem. Soc.* **2000**, *122*, 8319−8320.
(51) Pearson, R. G. Hard and Soft Acids and Bases. *J. Am. Chem. Soc.* **1963**, *85*, 3533−3539.
(52) Wang, L.; Li, D.-B.; Li, K.; Chen, C.; Deng, H.-X.; Gao, L.; Zhao, Y.; Jiang, F.; Li, L.; Huang, F.; He, Y.; Song, H.; Niu, G.; Tang, J. Stable 6%-efficient Sb_2Se_3 solar cells with a ZnO buffer layer. *Nat. Energy* **2017**, *2*, 17046.
(53) Li, Z.; Liang, X.; Li, G.; Liu, H.; Zhang, H.; Guo, J.; Chen, J.; Shen, K.; San, X.; Yu, W.; Schropp, R. E. I.; Mai, Y. 9.2%-Efficient Core-Shell Structured Antimony Selenide Nanorod Array Solar Cells. *Nat. Commun.* **2019**, *10*, 125.
(54) Nishikubo, R.; Kanda, H.; García-Benito, I.; Molina-Ontoria, A.; Pozzi, G.; Asiri, A. M.; Nazeeruddin, M. K.; Saeki, A. Optoelectronic and Energy Level Exploration of Bismuth and Antimony-Based Materials for Lead-Free Solar Cells. *Chem. Mater.* **2020**, *32*, 6416−6424.
(55) Fang, Y.; Yu, X.-Y.; Lou, X. W. Formation of Polypyrrole-Coated Sb_2Se_3 Microclips with Enhanced Sodium-Storage Properties. *Angew. Chem., Int. Ed.* **2018**, *57*, 9859−9863.
(56) Cui, C.; Xu, J.; Zhang, Y.; Wei, Z.; Mao, M.; Lian, X.; Wang, S.; Yang, C.; Fan, X.; Ma, J.; Wang, C. Antimony Nanorod Encapsulated in Cross-Linked Carbon for High-Performance Sodium Ion Battery Anodes. *Nano Lett.* **2019**, *19*, 538−544.
(57) Ma, Z.; Chai, S.; Feng, Q.; Li, L.; Li, X.; Huang, L.; Liu, D.; Sun, J.; Jiang, R.; Zhai, T.; Xu, H. Chemical Vapor Deposition Growth of High Crystallinity Sb_2Se_3 Nanowire with Strong Anisotropy for Near-Infrared Photodetectors. *Small* **2019**, *15*, 1805307.
(58) Park, J.; Yang, W.; Tan, J.; Lee, H.; Yun, J. W.; Shim, S. G.; Park, Y. S.; Moon, J. Hierarchal Nanorod-Derived Bilayer Strategy to Enhance the Photocurrent Density of Sb_2Se_3 Photocathodes for Photoelectrochemical Water Splitting. *ACS Energy Lett.* **2020**, *5*, 136−145.
(59) Won, J. K.; Hwang, C.; Ahn, K.; Choi, S.-Y.; Lee, Y.; Kim, J.; Lee, Y.; Park, S. K.; Chung, I.; Kim, C.; Kim, K.; Ahn, S. H.; Lee, M. H.; Kim, M.-G. Controlled synthesis of SnS_xSe_{2-x} nanoplate alloys via synergetic control of reactant activity and surface defect passivation control with surfactant and co-surfactant mixture. *J. Solid State Chem.* **2019**, *278*, 120887.
(60) Pangborn, A. B.; Giardello, M. A.; Grubbs, R. H.; Rosen, R. K.; Timmers, F. J. Safe and Convenient Procedure for Solvent Purification. *Organometallics* **1996**, *15*, 1518−1520.
(61) McCarthy, T. J.; Ngeyi, S. P.; Liao, J. H.; DeGroot, D. C.; Hogan, T.; Kannewurf, C. R.; Kanatzidis, M. G. Molten salt synthesis and properties of three new solid-state ternary bismuth chalcogenides, β-$CsBiS_2$, γ-$CsBiS_2$, and $K_2Bi_8Se_{13}$. *Chem. Mater.* **1993**, *5*, 331−340.

https://doi.org/10.1021/jacs.3c03925
J. Am. Chem. Soc. 2023, 145, 15951−15962

(62) Voutsas, G. P.; Papazoglou, A. G.; Rentzeperis, P. J.; Siapkas, D. The crystal structure of antimony selenide, Sb_2Se_3. *Z. Kristallogr. Cryst. Mater.* **1985**, *171*, 261−268.
(63) Zhou, Y.; Wang, L.; Chen, S.; Qin, S.; Liu, X.; Chen, J.; Xue, D.-J.; Luo, M.; Cao, Y.; Cheng, Y.; Sargent, E. H.; Tang, J. Thin-Film Sb_2Se_3 Photovoltaics with Oriented One-Dimensional Ribbons and Benign Grain Boundaries. *Nat. Photonics* **2015**, *9*, 409−415.
(64) Islam, S. M.; Peng, L.; Zeng, L.; Malliakas, C. D.; Chung, D. Y.; Buchholz, D. B.; Chasapis, T.; Li, R.; Chrissafis, K.; Medvedeva, J. E.; Trimarchi, G. G.; Grayson, M.; Marks, T. J.; Bedzyk, M. J.; Chang, R. P. H.; Dravid, V. P.; Kanatzidis, M. G. Multistates and Polymorphism in Phase-Change $K_2Sb_8Se_{13}$. *J. Am. Chem. Soc.* **2018**, *140*, 9261−9268.
(65) Pearson, R. G. Hard and Soft Acids and Bases, HSAB, part I: Fundamental Principles. *J. Chem. Educ.* **1968**, *45*, 581.
(66) Pearson, R. G. Hard and Soft Acids and Bases, HSAB, part II: Underlying Theories. *J. Chem. Educ.* **1968**, *45*, 643.
(67) Berlepsch, P.; Miletich, R.; Armbruster, T. The Crystal Structures of Synthetic KSb_5S_8 and $(Tl_{0.598}, K_{0.402})$ Sb_5S_8 and Their Relation to Parapierrotite ($TlSb_5S_8$). *Z. Kristallogr. Cryst. Mater.* **1999**, *214*, 57−63.
(68) Chen, W.-F.; Liu, B.-W.; Pei, S.-M.; Yan, Q.-N.; Jiang, X.-M.; Guo, G.-C. ASb_5S_8 (A = K, Rb, and Cs): Thermal Switching of Infrared Nonlinear Optical Properties across the Crystal/Glass Transformation. *Chem. Mater.* **2021**, *33*, 3729−3735.
(69) Kyratsi, T.; Chrissafis, K.; Wachter, J.; Paraskevopoulos, K. M.; Kanatzidis, M. G. KSb_5S_8: A Wide Bandgap Phase-Change Material for Ultra High Density Rewritable Information Storage. *Adv. Mater.* **2003**, *15*, 1428−1431.
(70) Yang, R. B.; Bachmann, J.; Pippel, E.; Berger, A.; Woltersdorf, J.; Gösele, U.; Nielsch, K. Pulsed Vapor-Liquid-Solid Growth of Antimony Selenide and Antimony Sulfide Nanowires. *Adv. Mater.* **2009**, *21*, 3170−3174.
(71) Mehta, R. J.; Karthik, C.; Jiang, W.; Singh, B.; Shi, Y.; Siegel, R. W.; Borca-Tasciuc, T.; Ramanath, G. High Electrical Conductivity Antimony Selenide Nanocrystals and Assemblies. *Nano Lett.* **2010**, *10*, 4417−4422.
(72) Kuykendall, T.; Ulrich, P.; Aloni, S.; Yang, P. Complete Composition Tunability of InGaN Nanowires Using a Combinatorial Approach. *Nat. Mater.* **2007**, *6*, 951−956.
(73) Chen, C.; Bobela, D. C.; Yang, Y.; Lu, S.; Zeng, K.; Ge, C.; Yang, B.; Gao, L.; Zhao, Y.; Beard, M. C.; Tang, J. Characterization of Basic Physical Properties of Sb_2Se_3 and Its Relevance for Photovoltaics. *Front. Optoelectron.* **2017**, *10*, 18−30.
(74) Lei, H.; Chen, J.; Tan, Z.; Fang, G. Review of Recent Progress in Antimony Chalcogenide-Based Solar Cells: Materials and Devices. *Sol. RRL* **2019**, *3*, 1900026.
(75) Zhai, T.; Ye, M.; Li, L.; Fang, X.; Liao, M.; Li, Y.; Koide, Y.; Bando, Y.; Golberg, D. Single-Crystalline Sb_2Se_3 Nanowires for High-Performance Field Emitters and Photodetectors. *Adv. Mater.* **2010**, *22*, 4530−4533.
(76) Chen, G.; Wang, W.; Wang, C.; Ding, T.; Yang, Q. Controlled Synthesis of Ultrathin Sb_2Se_3 Nanowires and Application for Flexible Photodetectors. *Adv. Sci.* **2015**, *2*, 1500109.
(77) Guo, C.; Liang, X.; Liu, T.; Liu, Y.; Yang, L.; Lai, W.; Schropp, R. E. I.; Song, D.; Mai, Y.; Li, Z. 1D/3D Alloying Induced Phase Transition in Light Absorbers for Highly Efficient Sb_2Se_3 Solar Cells. *Sol. RRL* **2020**, *4*, 2000054.
(78) Hobson, T. D. C.; Phillips, L. J.; Hutter, O. S.; Shiel, H.; Swallow, J. E. N.; Savory, C. N.; Nayak, P. K.; Mariotti, S.; Das, B.; Bowen, L.; Jones, L. A. H.; Featherstone, T. J.; Smiles, M. J.; Farnworth, M. A.; Zoppi, G.; Thakur, P. K.; Lee, T.-L.; Snaith, H. J.; Leighton, C.; Scanlon, D. O.; Dhanak, V. R.; Durose, K.; Veal, T. D.; Major, J. D. Isotype Heterojunction Solar Cells Using n-Type Sb_2Se_3 Thin Films. *Chem. Mater.* **2020**, *32*, 2621−2630.
(79) Qiu, W.; Zhang, C.; Cheng, S.; Zheng, Q.; Yu, X.; Jia, H.; Wu, B. The Crystal Structure, Electronic Structure and Photoelectric Properties of a Novel Solar Cells Absorber Material $Sb_2Se_{3-x}S_x$. *J. Solid State Chem.* **2019**, *271*, 339−345.
(80) Wu, C.; Lian, W.; Zhang, L.; Ding, H.; Jiang, C.; Ma, Y.; Han, W.; Li, Y.; Zhu, J.; Chen, T.; Zhu, C. Water Additive Enhanced Solution Processing of Alloy Sb_2 $(S_{1-x}Se_x)_3$-Based Solar Cells. *Sol. RRL* **2020**, *4*, 1900582.
(81) Hsu, K. F.; Loo, S.; Guo, F.; Chen, W.; Dyck, J. S.; Uher, C.; Hogan, T.; Polychroniadis, E. K.; Kanatzidis, M. G. Cubic $AgPb_mSbTe_{2+m}$: Bulk Thermoelectric Materials with High Figure of Merit. *Science* **2004**, *303*, 818−821.
(82) Lee, Y. K.; Ahn, K.; Cha, J.; Zhou, C.; Kim, H. S.; Choi, G.; Chae, S. I.; Park, J.-H.; Cho, S.-P.; Park, S. H.; Sung, Y.-E.; Lee, W. B.; Hyeon, T.; Chung, I. Enhancing p-Type Thermoelectric Performances of Polycrystalline SnSe via Tuning Phase Transition Temperature. *J. Am. Chem. Soc.* **2017**, *139*, 10887−10896.
(83) Lee, Y. K.; Luo, Z.; Cho, S. P.; Kanatzidis, M. G.; Chung, I. Surface Oxide Removal for Polycrystalline SnSe Reveals Near-Single-Crystal Thermoelectric Performance. *Joule* **2019**, *3*, 719−731.
(84) Lee, Y.-L.; Lee, H.; Kim, T.; Byun, S.; Lee, Y. K.; Jang, S.; Chung, I.; Chang, H.; Im, J. Data-Driven Enhancement of ZT in SnSe-Based Thermoelectric Systems. *J. Am. Chem. Soc.* **2022**, *144*, 13748−13763.
(85) Kim, H. S.; Choi, G.; Ha, M. Y.; Kim, D. H.; Park, S. H.; Chung, I.; Lee, W. B. Thermoelectric Transport Properties of Pb Doped SnSe Alloys ($Pb_xSn_{1-x}Se$): DFT-BTE Simulations. *J. Solid State Chem.* **2019**, *270*, 413−418.
(86) Quarez, E.; Hsu, K.-F.; Pcionek, R.; Frangis, N.; Polychroniadis, E. K.; Kanatzidis, M. G. Nanostructuring, Compositional Fluctuations, and Atomic Ordering in the Thermoelectric Materials $AgPb_mSbTe_{2+m}$. The Myth of Solid Solutions. *J. Am. Chem. Soc.* **2005**, *127*, 9177−9190.
(87) Kanatzidis, M. G. Nanostructured Thermoelectrics: The New Paradigm? *Chem. Mater.* **2010**, *22*, 648−659.
(88) Zhou, C.; Chung, I. Nanoscale defect structures advancing high performance n-type PbSe thermoelectrics. *Coord. Chem. Rev.* **2020**, *421*, 213437.
(89) Zhou, C.; Lee, Y. K.; Cha, J.; Yoo, B.; Cho, S.-P.; Hyeon, T.; Chung, I. Defect Engineering for High-Performance n-Type PbSe Thermoelectrics. *J. Am. Chem. Soc.* **2018**, *140*, 9282−9290.
(90) Zhou, C.; Yu, Y.; Lee, Y. K.; Cojocaru-Mirédin, O.; Yoo, B.; Cho, S.-P.; Im, J.; Wuttig, M.; Hyeon, T.; Chung, I. High-Performance n-Type PbSe-Cu_2Se Thermoelectrics through Conduction Band Engineering and Phonon Softening. *J. Am. Chem. Soc.* **2018**, *140*, 15535−15545.
(91) Zhou, C.; Yu, Y.; Lee, Y.-L.; Ge, B.; Lu, W.; Cojocaru-Mirédin, O.; Im, J.; Cho, S.-P.; Wuttig, M.; Shi, Z.; Chung, I. Exceptionally High Average Power Factor and Thermoelectric Figure of Merit in n-type PbSe by the Dual Incorporation of Cu and Te. *J. Am. Chem. Soc.* **2020**, *142*, 15172−15186.
(92) Ge, B.; Lee, H.; Zhou, C.; Lu, W.; Hu, J.; Yang, J.; Cho, S.-P.; Qiao, G.; Shi, Z.; Chung, I. Exceptionally Low Thermal Conductivity Realized in the Chalcopyrite $CuFeS_2$ via Atomic-Level Lattice Engineering. *Nano Energy* **2022**, *94*, 106941.
(93) Ge, B.; Lee, H.; Huang, L.; Zhou, C.; Wei, Z.; Cai, B.; Cho, S.-P.; Li, J.-F.; Qiao, G.; Qin, X.; Shi, Z.; Chung, I. Atomic Level Defect Structure Engineering for Unusually High Average Thermoelectric Figure of Merit in n-Type PbSe Rivalling PbTe. *Adv. Sci.* **2022**, *9*, 2203782.
(94) Cha, J.; Zhou, C.; Lee, Y. K.; Cho, S.-P.; Chung, I. High Thermoelectric Performance in n-Type Polycrystalline SnSe via Dual Incorporation of Cl and PbSe and Dense Nanostructures. *ACS Appl. Mater. Interfaces* **2019**, *11*, 21645−21654.
(95) Wang, S.; Sun, Y.; Yang, J.; Duan, B.; Wu, L.; Zhang, W.; Yang, J. High Thermoelectric Performance in Te-Free (Bi, Sb)$_2Se_3$ via Structural Transition Induced Band Convergence and Chemical Bond Softening. *Energy Environ. Sci.* **2016**, *9*, 3436−3447.
(96) Liu, X.; Wang, D.; Wu, H.; Wang, J.; Zhang, Y.; Wang, G.; Pennycook, S. J.; Zhao, L.-D. Intrinsically Low Thermal Conductivity in $BiSbSe_3$: A Promising Thermoelectric Material with Multiple Conduction Bands. *Adv. Funct. Mater.* **2019**, *29*, 1806558.

https://doi.org/10.1021/jacs.3c03925
J. Am. Chem. Soc. 2023, 145, 15951−15962

(97) Hernandez, J. A.; Fonseca, L. F.; Pettes, M. T.; Jose-Yacaman, M. Thermoelectric Properties of Antimony Selenide Hexagonal Nanotubes. *Nanotechnology* **2021**, *32*, 095705.
(98) Ko, T.-Y.; Shellaiah, M.; Sun, K. W. Thermal and Thermoelectric Transport in Highly Resistive Single Sb_2Se_3 Nanowires and Nanowire Bundles. *Sci. Rep.* **2016**, *6*, 35086.

https://doi.org/10.1021/jacs.3c03925
J. Am. Chem. Soc. 2023, 145, 15951−15962